Available online at www.sciencedirect.com
SCIENCE DIRECT®
Journal of Nuclear Materials 347 (2005) 244–254
journal of nuclear materials
www.elsevier.com/locate/jnucmat

Testing IFE materials on Z

Tina J. Tanaka [a,*], Greg A. Rochau [a], Robert R. Peterson [b], Craig L. Olson [a]

[a] Sandia National Laboratories, P.O. Box 5800, Albuquerque, NM 87185-1129, USA
[b] Los Alamos National Laboratory, P.O. Box 1663, Los Alamos, NM 87545, USA

Abstract

On a single-pulse basis, the tungsten armor for the chamber walls in a laser inertial fusion energy power plant must withstand X-ray fluences of 0.4–1.2 J/cm^2 with almost no mass loss, and preferably no surface changes. We have exposed preheated tungsten samples to 0.27 and 0.9 J/cm^2 X-ray fluence from the Z accelerator at Sandia National Laboratories to determine the single-shot X-ray damage threshold. Earlier focused ion beam analysis has shown that rolled powdered metal formed tungsten and tungsten alloys, will melt when exposed to 2.3 J/cm^2 on Z, but not at 1.3 J/cm^2. Three forms of tungsten – single-crystal (SING), chemical-vapor-deposited (CVD), and rolled powdered metal (PWM) – were exposed to fluence levels of 0.9 J/cm^2 without any apparent melting. However, the CVD and PWM sample surfaces were rougher after exposure than the SING sample, which was not roughened. BUCKY (1D) calculations show a threshold of 0.5 J/cm^2 for melting on Z. The present experiments indicate no melting but limited surface changes occur with polycrystalline samples (PWM and CVD) at 0.9 J/cm^2 and no surface changes other than debris for samples at 0.27 J/cm^2.

PACS: 61.82.Bg

1. Introduction

Chamber wall materials for laser inertial fusion energy (IFE) must withstand intense, short bursts of X-rays, ions, and neutrons from imploded targets. For the High Average Power Laser (HAPL) program, the X-ray fluence at a distance of 6.5 m for the low-yield (154 MJ) and high-yield (400 MJ) laser IFE targets is predicted to be 0.40 J/cm^2 and 1.2 J/cm^2, respectively [1]. X-rays in the energy range created by laser IFE targets will be absorbed on the chamber wall in a very thin layer (less than a micron in general). The X-ray energy converts primarily to heat that is deposited in a very short pulse of about 10 ns. This intense heat pulse can cause material to melt, or if energetic enough, vaporize and ablate, thinning the wall. Therefore a high melting point, high thermal conductivity material such as tungsten is considered for use as armor for the inner surface of the chamber walls. The purpose of this paper is to create a relevant single-X-ray pulse in the Z accelerator at Sandia National

* Corresponding author. Tel.: +1 505 844 2981; fax: +1 505 845 3130.
E-mail address: tjtanak@sandia.gov (T.J. Tanaka).

0022-3115/$ - see front matter © 2005 Elsevier B.V. All rights reserved.
doi:10.1016/j.jnucmat.2005.08.016

Laboratories[1] and determine whether the candidate wall materials, in particular, tungsten, can withstand the irradiation.

We have been unable to find any X-ray ablation studies on tungsten. The majority of the literature on X-ray ablation is on plastics and lower melting point metals, such as gold and aluminum, that are easily ablated [2–4].

Tungsten is a prime candidate in similar studies conducted for magnetic fusion energy (MFE) [5,6]. For tokamaks, and many other types of MFE devices a steady flux of X-rays and plasma particles are expected, however, short term events are also expected to intensely heat the plasma facing components. The related research on short term events on heat loads and materials response may be directly relevant to or at least complementary to that needed for IFE. For example, in an MFE disruption event, there is a loss of stability of the plasma in which the plasma moves rapidly towards the chamber surface, causing heating similar to that of an IFE event. In Edge Localized Modes, or ELMs, particles and energy are lost from the plasma edge in repeated 'bursty' events. For example, Type I (large) ELMs projected for ITER may not be tolerable and have a nominal feature for their estimated heat load of a triangular wave pulse with a 300 μs ramp up to a $5GW/m^2$ peak heat load and a 300 ms ramp down [7–12]. This is an area of active interest in the MFE community with many papers in the recent International Conference on Plasma Surface Interactions [13].

Ablation studies for the National Ignition Facility (NIF) were conducted to determine the response of proposed first wall materials to X-rays generated from a hohlraum target. The hohlraum was excited by laser shots on Nova. The materials for these tests included fused silica, silicon nitride, aluminum, aluminum oxide, boron carbide, boron, silicon carbide, and amorphous carbon [14]. Experiments were accompanied by a modeling effort that included X-ray energy deposition, heat conduction, hydrodynamics, and surface vaporization.

Matching the expected X-ray spectrum and pulse length is important because these parameters determine how deep the energy is deposited into the surface of the material, and whether the thermal conductivity can help diffuse the energy away before the material melts. Given the same total fluence, a low-energy X-ray pulse will ablate more of the surface than a high energy X-ray pulse, because more of the energy is absorbed in the top surface layer. Because the X-ray pulse is short, the thermal conductivity may not be high enough to transport the heat from the surface during the pulse. The shorter the pulse, the higher the surface layer temperature will be. To replicate the laser IFE X-ray dose, it would be best to replicate both the spectrum and pulse length.

To qualify materials for use in a laser IFE chamber, candidate materials are being exposed to X-rays on the Z accelerator at Sandia National Laboratories [15]. Z produces X-rays by flowing large currents through a Z-pinch target consisting of an array of tungsten wires. The spectrum of the X-rays from Z (peak at 0.6 keV) is somewhat softer than the spectrum expected from the direct-drive laser IFE targets (peak at 4 keV).

Our earlier work on Z focused on materials such as Poco graphite and carbon velvet in addition to tungsten [16,17]. When Poco graphite was exposed to $6\ J/cm^2$ of X-rays, pieces of carbon are removed from the surface, but there was no general surface level erosion. At 10 Hz there are 3×10^8 shots per year so we can not afford to lose even the slightest amount of material per shot. Therefore, we are actually looking for a null effect; i.e., to find a threshold of X-ray fluence below which there is no effect to the wall material by either ablation or roughening. Prior to exposures Z machine samples are polished so that changes in the surface can be better measured. After the exposure, the exposed areas are compared to unexposed areas using a surface profilometer to measure average roughness, R_a. There is a problem inherent to this method in Z, debris that deposits on samples near the end of the shot also cause roughness on the sample.

For melting, the differences of pulse length and spectrum are critical to knowing if material will melt. Since Z will not precisely replicate the HAPL targets, it is important that we calculate the melt and confirm the calculation with Z experimental data. Calculations on vaporization and melt are presented for the Z experimental data using test conditions. Melt thresholds for the case of the actual HAPL target can then be calculated.

For roughening, our improved diagnostics are now able to see surface pitting and cracking and establish a threshold for roughening. The theory for these roughening effects is being studied [18], and the effects of multiple shots on roughening are

[1] Sandia is a multi-program laboratory operated by Sandia Corporation, a Lockheed Martin Company, for the United States Department of Energy's National Nuclear Security Administration under contract DE-AC04-94AL85000.

being examined on the XAPPER facility at Lawrence Livermore National Laboratory [19].

2. Experiment

2.1. The Z pulsed power accelerator as a source of X-rays

The Z pulsed power accelerator (Fig. 1) at Sandia National Laboratories is the world's most powerful laboratory X-ray source. Z drives a peak current of up to 20 MA through a tungsten wire array similar to the array shown in Fig. 2. The high current ionizes the wires, and the magnetic fields that are produced by the currents forces the wire material to pinch in on itself, creating a high density plasma. The plasma produces X-rays whose spectrum depends on the plasma temperature, density and composition. Tungsten 'dynamic hohlraum' wire arrays were used in all of the shots for these X-ray exposures [20]. In general, tungsten arrays produce a fairly smooth spectrum with few characteristic lines Figs. 3 and 4.

The X-ray output of Z is measured with a variety of detectors that have different ranges of sensitivity. The primary diagnostics for the X-ray energy range relevant to laser IFE are filtered X-ray diodes [21]. An array of filtered X-ray diodes are fielded on each shot, some along the line of sights, similar to the sample location, and some along the axis of the pinch. Other diagnostics include filtered bolometers [22], filtered photoconductive detectors [23] and a transmission grating spectrograph [24]. Time-dependent spectra are unfolded from the various diagnostics to

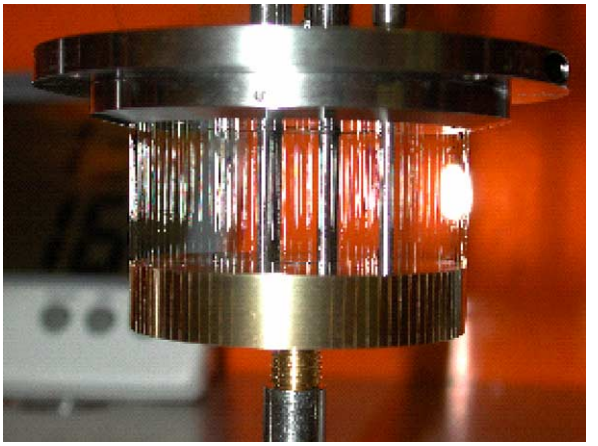

Fig. 2. A tungsten wire array with 144 thin tungsten wires.

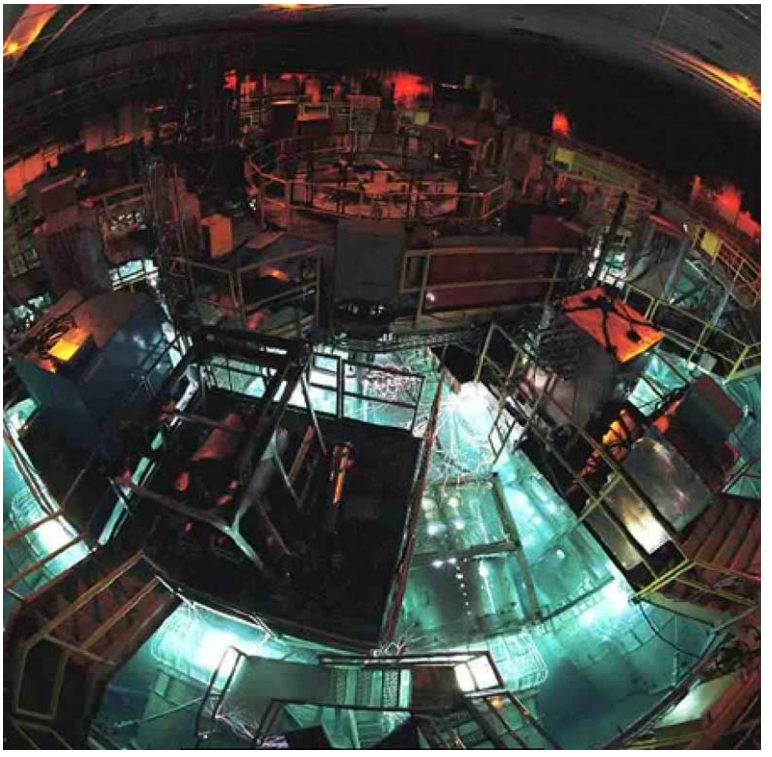

Fig. 1. Z pulsed power accelerator at Sandia National Laboratories.

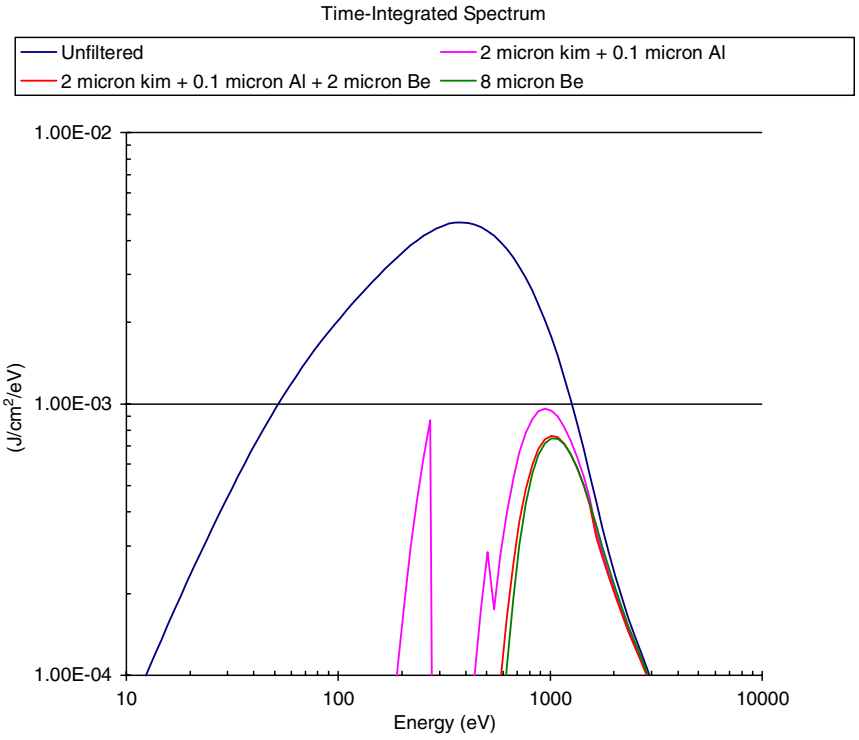

Fig. 3. The X-ray spectrum of the aperture Z-pinch is modified by filtering.

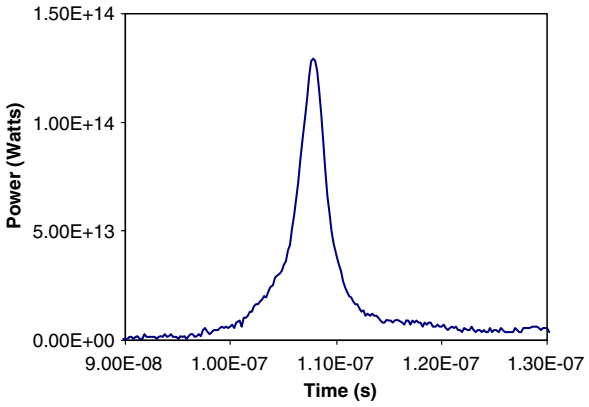

Fig. 4. Time history of the Z-pinch X-ray pulse.

derive the 'black body' equivalent temperatures. At the peak of intensity, the spectrum can be modeled with a 300 eV black body combined with a 10% contribution from a 600 eV black body [20].

The X-ray spectrum for the HAPL target (154 MJ) is presented in this issue [25]. To fit the HAPL spectrum, the Z-pinch spectrum can be tailored to higher peak energy by filtering out low-energy X-rays and varying the distance from the target. Filtering is best with low-Z filters such as beryllium or carbon because they have fewer absorption edges in the range of X-ray energies we wish to preserve. We can determine the distance from the target that best fits both the spectrum and the total flux when compared to the laser IFE targets. Of course, the final laser IFE targets may produce a different spectrum or fluence than calculated. Therefore it is important to test a range of fluence and spectra. Fluences were varied by changing filters and distances to the sample. To provide for a worst case in terms of armor, a higher fluence than expected and a softer spectrum (lower energy X-rays) would cause more surface damage because it would localize the heat deposition to the surface.

2.2. Samples, sample placement, shielding, and heating

Samples of tungsten included polished single-crystal, polished rolled powdered metal, and chemical vapor deposited tungsten [26]. One each of these samples was exposed on each of three shots, behind common filters, and all located at the same distance from the source. Typically we have placed the samples ≈70 cm from the source in the center section of the accelerator. There is enough fluence at this

close distance to be able to replicate the HAPL spectrum (a higher average energy than what is on Z) by filtering out the low energy X-rays, and still obtain a fluence that is close to that expected for HAPL. A one-meter diameter cylindrical steel blast shield surrounds the source of the Z-pinch machine with slots for the various lines of sight. The blast shield serves to protect some of the vacuum chamber, but in doing so, it also re-radiates some X-ray energy. To eliminate some of this distributed radiation, the samples are placed in thick stainless steel box to reduce scatter and collimate the beam. A schematic of the shielding box is shown in Fig. 5. In the latest shots, an additional aperture was placed between the shielding box and the source to reduce the scatter from the current return can and blast shield. We calculate the total spectrum from the Z-pinch, Z-pinch hardware, apertures and shield box using a view-factor model. Approximately 98% of the spectrum when using the aperture is from the Z-pinch alone.

Another advantage to using the shielding box is that it reduces debris on the samples. Early tests done in this program featured uncollimated samples. The collimation reduces, but cannot eliminate the debris on the sample. Debris from Z consists of material from the wire array and target, the framework that holds the wire array and conducts the current into the array, and filter material that was used to adjust the spectrum. Samples were evaluated in a scanning electron microscope (SEM) to determine what elements are contained in the debris from Z. Poco graphite samples have shown little tungsten debris and thus the wire array is not a large contributor to the debris on the surface of samples. The majority of material in the debris appears to contain stainless steel – the material that holds the target array and is the final conductor into the array. Substantial amounts of filter materials can also be found on samples. Because of the addition of debris on samples, it is not practical to use mass loss as a measure of damage.

The wall of the reactor chamber will not cool down to room temperature between shots. To get a more realistic simulation of the X-ray effect on the wall material, the armor material was preheated with a small vacuum-compatible button heater to 600 °C. The elevated temperature can be helpful for materials such as tungsten because tungsten is more brittle at room temperatures than above the brittle-ductile transition of about 400 °C.

Fig. 6 shows the sample heater mounted in an aluminum box that holds the filters. This aluminum box fits inside of the stainless steel shielding box. The samples were clipped to the front of the sample heater. The heater was controlled by a feedback

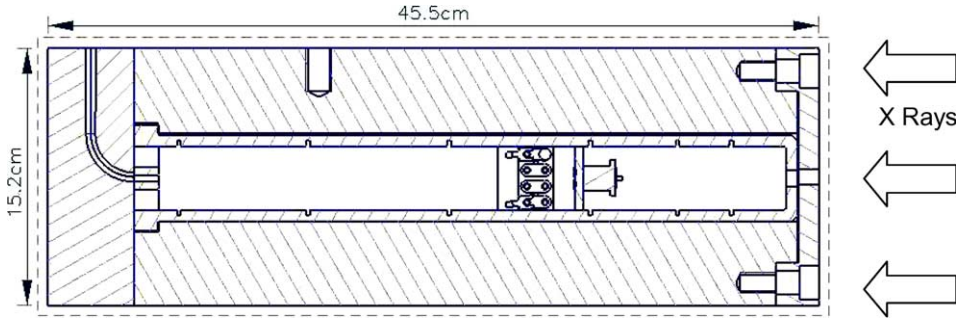

Fig. 5. Schematic of shielding box. Most of the shielding material is stainless steel.

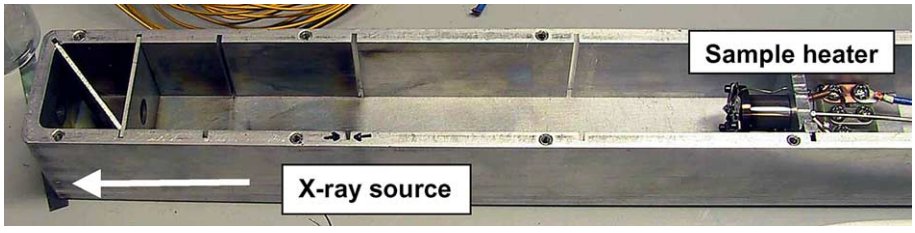

Fig. 6. Inner box that fits inside shielding box. This holds filters, sample, and sample heater.

loop from a thermocouple located in the vicinity of the samples.

2.3. Surface damage diagnostics

X-rays are absorbed by and heat the armor. If enough energy is deposited, the material will melt, vaporize, and perhaps be blown away from the wall (ablation). Roughening of tungsten surfaces has also been observed from ion beam exposures [27] without changes in average surface height. Because of the number of pulses that are expected in an IFE full power year (3×10^8 for 10 Hz), qualification of the armor material requires that loss of material on one shot is near zero. Even an atomic monolayer would be problematic. Our early efforts at analysis included weighing samples before and after the shots, surface profiling with a stylus, and cross sections with SEM. These methods are not accurate enough to measure mass loss on a single-shot basis. Debris from Z increases weight of the sample more than the allowed amount of material that can be lost per shot. Surface profiles show many rough features, but not a uniform step, as the material is often cracked, and debris can increase the surface level. The following describes more in-depth analysis methods that may yield better threshold values.

The surface melting on the order of a micron can be observed using focused ion beam (FIB) milling and subsequent imaging [28]. One can observe changes in grain boundaries as a result of melting and resolidification. Earlier work on unheated samples with fluences above 2.3 J/cm^2 have shown that PWM tungsten samples originally with flat pancake grains, solidify to columnar grains after melting as shown in Fig. 7. To produce this image, the FIB mills a ramp-like shape into the tungsten surface by accelerating a narrow beam of gallium ions at the surface and sputtering the tungsten away. The cut-out in the sample is about 10 μm deep with a smooth surface perpendicular to the exposed face. The FIB is then used with a secondary electron detector to image the grain structure. This method can be used to observe grain changes down to the size of a typical grain height, in the case of PWM, ≈0.2 μm.

Even smaller changes of the surface were observed by carefully combining various methods of imaging. High magnification surface profiling with a white light interferometer was used to measure the variation in surface height down to 50 nm. The scanning

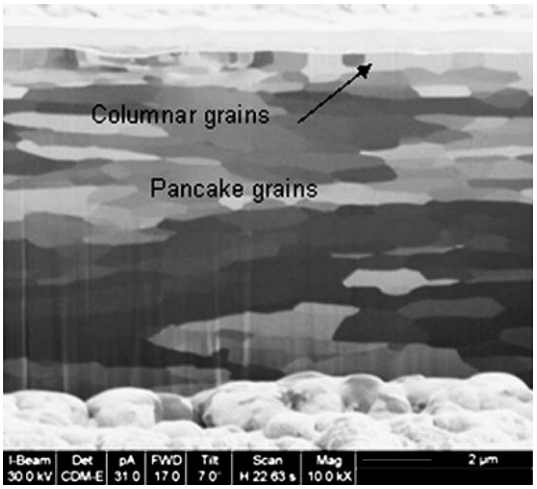

Fig. 7. FIB cross-section image of PWM sample exposed to 2.3 J/cm^2. The top 0.5 μm was melted.

electron microscope (SEM) was then used to help identify debris as opposed to surface roughness. Care was taken that the same areas were scanned by the two methods, as the images appeared vastly different. Using the standard secondary electron detector, the SEM image appear bright where there are edges where secondary electrons escape easily or where there was a high density material. Elemental analysis with the SEM and the X-ray detector determined the composition of the debris from the Z-pinch target area. Further analysis in the SEM with the backscatter electron detector (BSE) was used to determine the location of beryllium on the surfaces of the tungsten.

2.4. BUCKY calculation of expected melt depths

The BUCKY [29] computer code has been used to model the experiments discussed in this paper. BUCKY is a one-dimensional Lagrangian radiation hydrodynamics computer code. The code includes time and energy-dependent deposition of X-rays. The code calculates heat transfer in materials via thermal diffusion and multi-group radiation diffusion to produce time-dependent temperature profiles in a material irradiated with X-rays from Z. Temperature dependent thermal properties are used in the thermal diffusion calculation. The heat of fusion is included in the temperature-dependent heat capacity and the properties of molten tungsten are used above the melting temperature [30]. BUCKY can be used to determine the melt threshold, but cannot predict surface roughening effects (which are multi-dimensional effects).

3. Results

3.1. Tungsten results

Polished samples of tungsten that were preheated to 600 °C and exposed to X-rays on the Z accelerator were analyzed by FIB imaging, optical surface profiling, and SEM. Although FIB images before and after exposure showed no changes for either 0.27 or 0.9 J/cm^2, optical surface measurements show significant changes between the exposed surfaces and unexposed surfaces. These changes are shown in Figs. 8(a), 9(a), and 10(a), where the right sides were unexposed and the left sides were exposed at 0.9 J/cm^2. The right sides do show some machining or manufacturing lines, but these lines are obscured on the left side by the changes due to the exposure. Further magnification of the surface reveal differences in the PWM, CVD and SING samples as shown in Figs. 8(b), 9(b), and 10(b). The artificial coloring in the high magnification images indicates the various heights on the sample as indicated by the scale to the right of these figures. Although the three samples were all exposed on the same shot and behind the same filter, the polycrystalline samples (PWM and CVD) are much rougher after exposure than the single-crystal sample (which was not roughened). The PWM and CVD have areas that look low compared to the average whereas the debris only sits on the surface of the SING sample. Single crystal tungsten appears to be more robust to X-rays at 0.9 J/cm^2.

Two types of changes were found from these exposures: (1) deposition of debris and (2) changes to the surface of the tungsten due to the intense X-ray pulse. The debris consist of materials emitted from the target area of the Z accelerator, primarily steel that deposit as the larger drops on the exposed

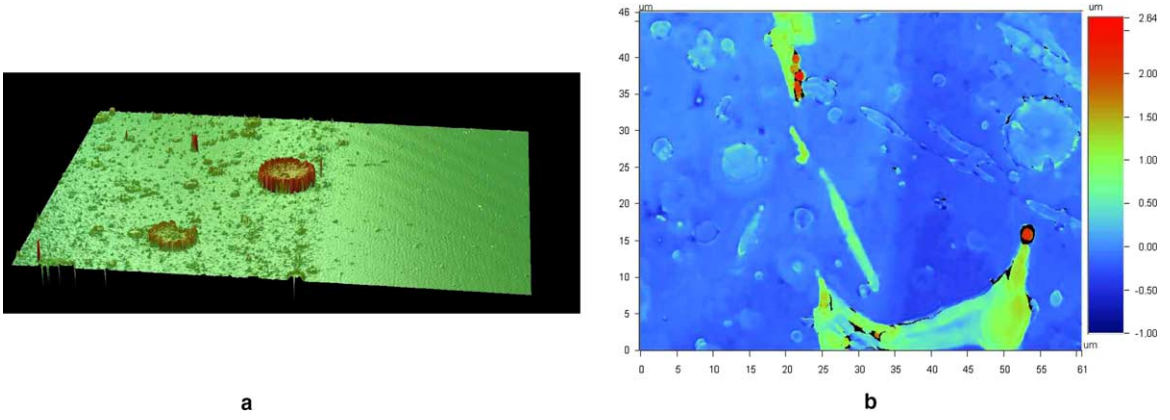

Fig. 8. (a) SING, 0.9 J/cm^2, the exposed left side shows the effects of debris, but no surface roughening (1.2 mm × 0.92 mm) and (b) image on right is a magnification of exposed area.

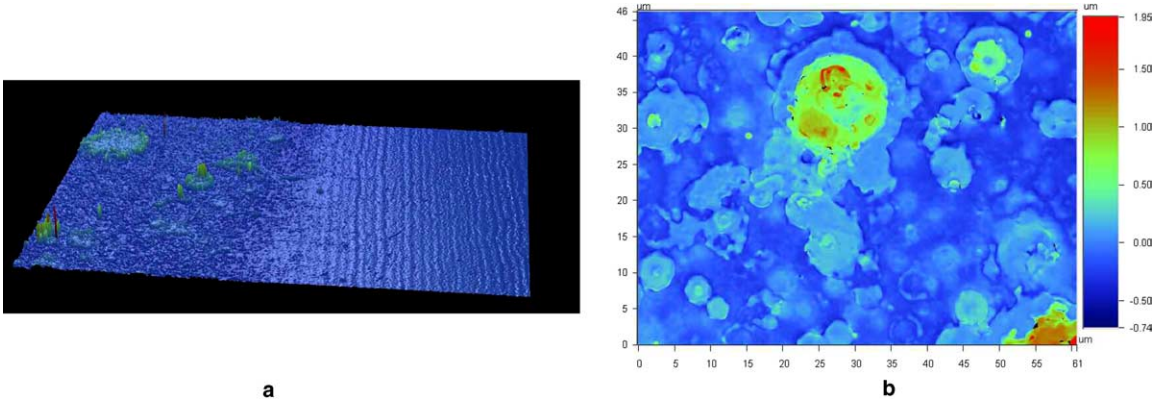

Fig. 9. (a) PWM, 0.9 J/cm^2, surface profile, (1.2 mm × 0.92 mm), the exposed left side shows debris and surface roughening. (b) High magnification surface profile of exposed PWM.

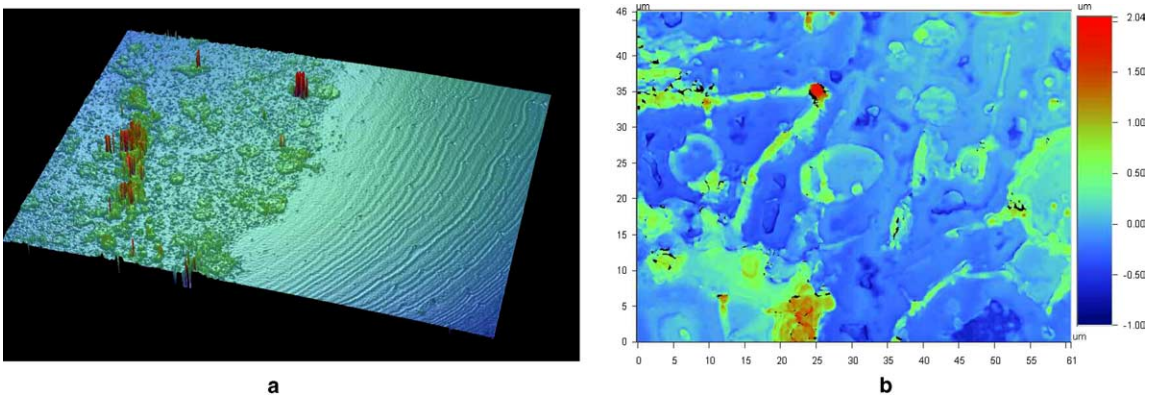

Fig. 10. (a) CVD, 0.9 J/cm^2, (1.2 mm × 0.92 mm), the exposed left side shows debris and surface roughening. (b) High magnification surface profile of exposed CVD shows some low areas between debris.

areas, and beryllium, the material that was used for filtering the X-rays. The steel debris is easily identified by an X-ray detector in the SEM. Fig. 11 shows an SEM image of almost the same area and scale as the surface profile image in Fig. 8. The dark areas on the SEM are due to the iron, copper and nickel from the steel. X-ray analysis of the white areas on the SEM image indicate only the presence of tungsten, but an image using a backscatter detector shows that they are a combination of tungsten and beryllium. Molten beryllium alloys easily with tungsten, so the filter material adds significantly to the debris on the sample.

For 0.9 J/cm^2 of exposure, the rolled and CVD samples have rougher surfaces than the single-crystal tungsten even though they were all fielded behind the same filters and exposed at the same distance from the same Z accelerator shot. At 0.27 J/cm^2, the differences in roughening between the three materials is much less pronounced. Fig. 12 summarizes the roughening in the three materials for different X-ray exposures.

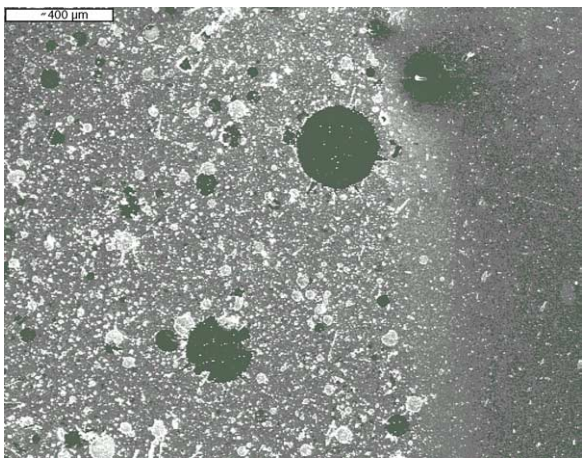

Fig. 11. SEM image of single-crystal, same area as Fig. 8.

3.2. BUCKY calculation results

Calculations have been performed to model tungsten initially at room temperature irradiated with X-rays from the Z accelerator. The X-rays in the experiments pass through 8 μm of beryllium, which is included in the BUCKY model. We have used BUCKY to predict melt depths versus fluence. The results for these calculations are summarized in Table 1. Note that at about 10 J/cm^2 of unfiltered fluence, the tungsten begins to vaporize. The vapor produced provides additional filtering that reduces the fluence actually depositing in the solid tungsten. This is shown in Fig. 13, where the fluence filtered by the beryllium and the fluence deposited in the solid are plotted against unfiltered fluence. When there is substantial vaporization the fluence reaching the solid is reduced. There is very little heat transfer between the vapor and the solid, though BUCKY does include this. In Fig. 14, the melt and vaporization depths are plotted against the fluence after beryllium filtering. BUCKY predicts that the melting threshold for tungsten is about 0.5 J/cm^2 of filtered X-rays and the vaporization threshold is about 2.4 J/cm^2.

Experimental results of melting are presented in Table 2. Comparisons of BUCKY to the experimental results are shown in Fig. 15. The error bars shown on are estimated from the grain size of the tungsten and

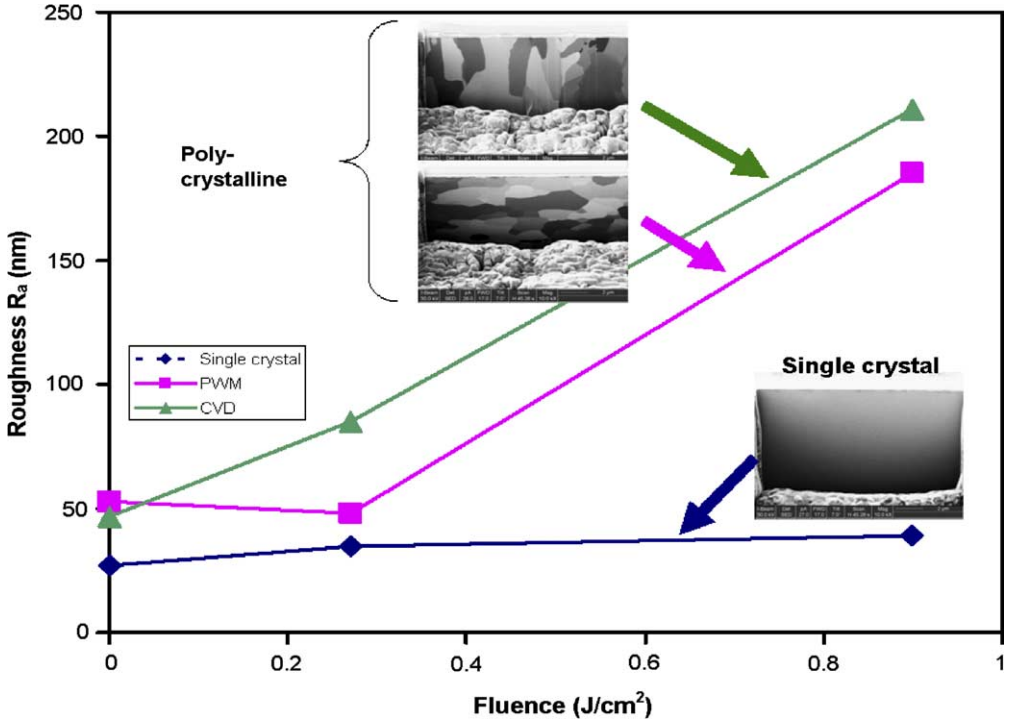

Fig. 12. Roughening versus fluence for single-crystal, rolled powder metal and chemical vapor deposition tungsten.

Table 1
BUCKY predictions of melt depths produced by Z X-rays

Unfiltered X-ray fluence (J/cm^2)	Filtered X-ray fluence (J/cm^2)	Fluence deposited in solid (J/cm^2)	Melt depth (μm)	Vapor depth (μm)
2.01	0.50	0.50	0	0
4.36	1.08	1.08	0.25	0
9.76	2.42	2.30	0.547	0.0655
12.0	2.99	2.68	0.604	0.108
31.6	7.86	5.03	0.721	0.386
60.0	14.9	6.89	0.805	0.623

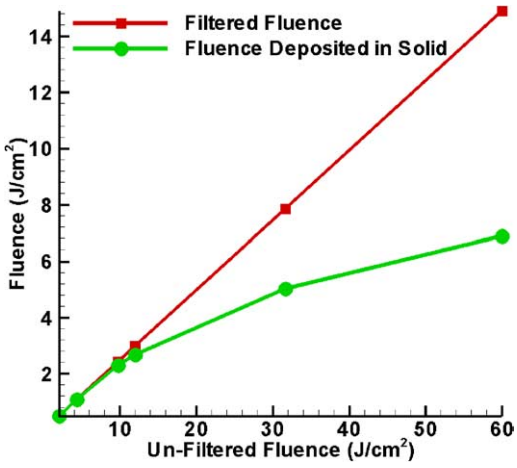

Fig. 13. BUCKY calculation of filtered fluence and fluence deposited in the solid versus filtered fluence.

how closely we expect to be able to estimate the melt depth. The experimental measurements show that melting will occur at higher fluence levels than is predicted by BUCKY. There are many sources of error that can be attributed to these differences. First of all, BUCKY uses thermal conductivity, a bulk property, and does not account for the individual grains and other possible surface effects. Like the FIB images, X-rays may well travel through some grain orientations more easily than others. Secondly, it is experimentally difficult to measure very small melt depths. The vaporization threshold is not measured experimentally as it is difficult to determine loss of these small amounts of material.

BUCKY simulations for the HAPL target calculate a tungsten ablation (vaporization) threshold of

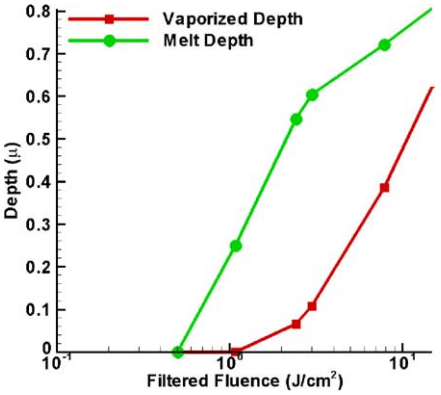

Fig. 14. BUCKY calculation of melt depth of tungsten irradiated with Z X-rays versus filtered fluence.

Table 2
Comparison of results for rolled powdered metal tungsten

Fluence (J/cm^2)	Preheat	Filter	Melt level
19	No	None	1.5 μm
2.3	No	2 μm kimfoil + 0.1 μm Al	0.5 μm
1.3	No	2 μm kimfoil + 0.1 μm Al + 2.5 μm Be	None
0.9	600 °C	8 μm Be + aperture	None

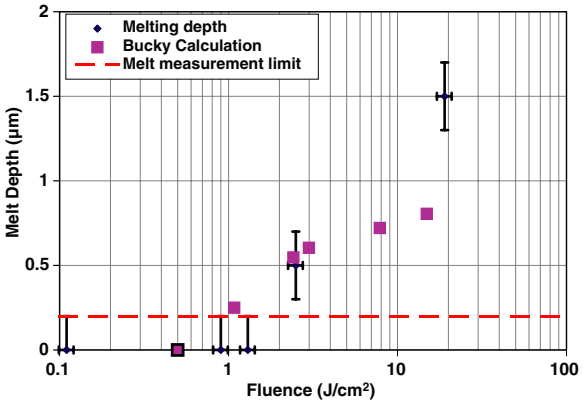

Fig. 15. Melt depth versus fluence for experimental points (error bars) and BUCKY calculation (squares) using filtered fluence numbers. For melt depths <0.2 μm, as indicated by the dashed line, the melt depth is less than the crystal grain size, and may or may not result in an observable effect.

3.5–4.0 J/cm^2[1]. This value is higher than the threshold calculated for vaporization on Z (2.4 J/cm^2) because the HAPL spectrum is harder and the heat deposits deeper into the material. The predicted level of fluence for the high yield target is 1.2 J/cm^2, so according to the BUCKY calculation there should be no vaporization.

4. Conclusions

Differences between the roughness of single-crystal and polycrystalline samples of tungsten indicate that at 0.9 J/cm^2, the polycrystalline samples are roughened by X-rays. BUCKY simulations for this level of fluence indicate that 0.2 μm of material should have melted, however no melting was observed for these samples using FIB imaging. At 0.27 J/cm^2 very little roughening is observed in all three types of tungsten, therefore the threshold for roughening for X-rays for polycrystalline tungsten is between 0.27 and 0.9 J/cm^2, and for single-crystal tungsten is above 0.9 J/cm^2. The grain boundaries are significant to determining the roughening threshold. The theory of roughening is being studied [18] and the effects of multiple X-ray exposures will be examined using XAPPER [19].

Acknowledgements

The authors would like to thank Nathan Joseph for fielding these experiments in Z and Michael Rye for providing the focused ion beam images. Justin Stolp of Schaefer Corporation provided the 2D surface profiles. This work was supported by NRL through the HAPL Program by the US Department of Energy, NNSA, DP.

References

[1] J.D. Sethian, M. Friedman, R.H. Lehrnberg, et al., Nucl. Fus. 43 (2003) 1693.
[2] B.A. Hammel, R.J. Wallace, D.W. Phillion, T.S. Perry, H.N. Kornblum, B.A. Remington, D. Munro, J.D. Kilkenny, Phys. Plasmas 1 (5) (1994) 1662.
[3] L. Juha, J. Krása, A. Präg, A. Cejnarová, D. Chvostová, K. Rohlena, K. Jungwirth, J. Kravárik, P. Kubeš, Y.L. Bakshaev, A.S. Chernenko, V.D. Korolev, V.I. Tumanov, M.I. Ivanov, A. Bernardinello, J. Ullschmied, F.P. Boody, Surf. Rev. Lett. 9 (1) (2002) 347.
[4] T. Endo, H. Shiraga, K. Shihoyama, Y. Kato, Phys. Rev. Lett. 60 (11) (1988) 1022.
[5] Naoaki Yoshida, J. Nucl. Mater. 266–269 (1999) 197.
[6] T. Tanabe, V. Philipps, K. Nakamura, M. Fujine, Y. Ueda, M. Wada, B. Schweer, A. Pospieszyk, B. Unterberg, J. Nucl. Mater. 241–243 (1997) 1164.
[7] G. Federici, A. Loarte, G. Strohmayer, Plasma Phys. Controlled Fus. 45 (2003) 1523.
[8] A.W. Leonard, A. Herrmann, K. Itami, J. Lingertat, A. Loarte, T.H. Osborne, W. Suttrop, J. Nucl. Mater. 269 (1999) 109.

[9] B.N. Bazylev et al., J. Nucl. Mater. 337–339 (1–3 Sp. Iss.) (2005) 766.
[10] M. Becoulet et al., J. Nucl. Mater. 337–339 (1–3 Sp. Iss.) (2005) 677.
[11] G. Federici et al., J. Nucl. Mater. 337–339 (2005) 684.
[12] I.S. Landman et al., J. Nucl. Mater. 337–339 (1–3 Sp. Iss.) (2005) 761.
[13] www.psfc.mit.edu/psi16.
[14] A.T. Anderson, A.K. Burnham, M.T. Tobin, P.F. Peterson, Fus. Tech. 30 (1996) 757.
[15] W.A. Stygar, H.C. Ives, D.L. Fehl, M.E. Cuneo, M.G. Mazarakis, J.E. Bailey, G.R. Bennett, D.E. Bliss, G.A. Chandler, R.J. Leeper, M.K. Matzen, D.H. McDaniel, J.S. McGurn, J.L. McKenney, L.P. Mix, D.J. Muron, J.L. Porter, J.J. Ramirez, L.E. Ruggles, J.F. Seamen, W.W. Simpson, C.S. Speas, R.B. Spielman, K.W. Struve, J.A. Torres, R.A. Vesey, T.C. Wagoner, T.L. Gilliland, M.L. Horry, D.O. Jobe, S.E. Lazier, J.A. Mills, T.D. Mulville, J.H. Pyle, T.M. Romero, J.J. Seamen, R.M. Smelser, Phys. Rev. E. 69 (2004) 046403.
[16] T.J. Renk, C.L. Olson, T.J. Tanaka, M.A. Ulrickson, G.A. Rochau, R.R. Peterson, I.E. Golovkin, M.O. Thompson, T.R. Knowles, A.R. Raffray, M.S. Tillack, Fus. Eng. Des. 65 (2003) 399.
[17] K. Kasuya, A. Kasamatsu, Y. Kinoshita, T. Kamiya, A. Saiki, T.J. Renk, C.L. Olson, J. Nucl. Mater. 313–316 (2003) 235.
[18] J.P. Blanchard, C.J. Martin, J. Nucl. Mater., these Proceedings, doi:10.1016/j.jnucmat.2005.08.007.
[19] J. Latkowski et al., J. Nucl. Mater., these Proceedings, doi:10.1016/j.jnucmat.2005.08.018.
[20] T.W.L. Sanford, R.W. Lemke, R.C. Mock, G.A. Chandler, R.J. Leeper, C.L. Ruiz, D.L. Peterson, R.E. Chrien, G.C. Idzorek, R.G. Watt, J.P. Chittenden, Phys. Plasmas 9 (8) (2002) 3573.
[21] G.A Chandler, C. Deeney, M. Cuneo, D.L. Fehl, J.S. McGurn, R.B. Spielman, J.A. Torres, J.L. McKenney, J. Mills, K.W. Stuve, Rev. Sci. Inst. 70 (1999) 561.
[22] R.B. Spielman, C. Deeney, D.L. Fehl, D.L. Hanson, N.R. Keltner, J.S. McGurn, J.L. McKenney, Rev. Sci. Inst. 70 (1) (1999) 651.
[23] T.W.L. Sanford, T.J. Nash, R.C. Mock, R.B. Spielman, J.F. Seamen, J.S. McGurn, D. Jobe, T.L. Gilliland, M. Vargas, K.G. Whitney, J.W. Thornhill, P.E. Pulsifer, J.P. Apruzese, Rev. Sci. Inst. 68 (1) (1997) 852.
[24] L.E. Ruggles, M.E. Cuneo, J.L. Porter, D.F. Wenger, W.W. Simpson, Rev. Sci. Inst. 72 (1) (2001) 1218.
[25] A. Raffray et al., J. Nucl. Mater., these Proceedings, doi:10.1016/j.jnucmat.2005.08.015.
[26] Samples provided by Lance Snead of Oak Ridge National Laboratory.
[27] T.J. Renk et al., J. Nucl. Mater., these Proceedings, doi:10.1016/j.jnucmat.2005.08.021.
[28] J. Orloff, M. Utlaut, L. Swanson, High Resolution Focused Ion Beams: FIB and Its Applications, Kluwer Academic/Plenum, New York, 2003, ISBN 0-306-47350-X (303 pp.).
[29] R.R. Peterson et al., Fus. Technol. 30 (1996) 783.
[30] T.J. Tanaka, private communication, 2003.